STEREO SCIENCE RESULTS AT SOLAR MINIMUM

On the Origin, 3D Structure and Dynamic Evolution of CMEs Near Solar Minimum

H. Xie · O.C. St. Cyr · N. Gopalswamy · S. Yashiro · J. Krall · M. Kramar · J. Davila

Abstract We have conducted a statistical study 27 coronal mass ejections (CMEs) from January 2007 – June 2008, using the stereoscopic views of STEREO SECCHI A and B combined with SOHO LASCO observations. A flux-rope model, in conjunction with 3D triangulations, has been used to reconstruct the 3D structures and determine the actual speeds of CMEs. The origin and the dynamic evolution of the CMEs are investigated using COR1, COR2 and EUVI images. We have identified four types of solar surface activities associated with CMEs: *i*) total eruptive prominence (totEP), *ii*) partially eruptive prominence (PEP), *iii*) X-ray flare, and *iv*) X-type magnetic structure (X-line). Among the 27 CMEs, 18.5% (5 of 27) are associated with totEPs, 29.6% (8 of 27) are associated with PEPs, 26% (7 of 27) are flare related, and 26% (7 of 27) are associated with X-line structures, and 43% (3 of 7) are associated with both X-line structures and PEPs. Three (11%) could not be associated with any detectable activity. The mean actual speeds for totEP-CMEs, PEP-CMEs, flare-CMEs, and X-line-CMEs are 404 $\mathrm{km\,s^{-1}}$, 247 $\mathrm{km\,s^{-1}}$, 909 $\mathrm{km\,s^{-1}}$, and 276 $\mathrm{km\,s^{-1}}$, respectively; the average mean values of edge-on and broadside widths for the 27 CMEs are 52 and 85 degrees, respectively. We found that slow CMEs ($V \leq 400\ \mathrm{km\,s^{-1}}$) tend to deflect towards and propagate along the streamer belts due to the deflections by the strong polar magnetic fields of corona holes, while some faster CMEs show opposite deflections away from the streamer belts.

H. Xie (✉) · S. Yashiro · M. Kramar
The Catholic University of America, Washington, DC, USA
e-mail: hong.xie@nasa.gov

O.C. St. Cyr · N. Gopalswamy · J. Davila
NASA Goddard Space Flight Center, Greenbelt, MD, USA

J. Krall
Plasma Physics Division, Naval Research Laboratory, Washington, DC, USA

Keywords Corona mass ejections · 3D reconstruction · Flux rope model fit

1. Introduction

White-light coronagraphs such as the Large Angle and Spectrometric Coronagraph (LASCO; Brueckner *et al.*, 1995) detect CMEs by measuring the photospheric light Thomson-scattered by electrons in the coronal plasma. Since the corona is optically thin, corona-graph images can only detect the integrated intensity along the line of sight (LOS), pro-viding two-dimensional projections of CMEs on the plane of the sky (POS). The shapes and sizes of CMEs as seen in coronagraph images vary from event to event depending on the CME orientations and locations. Different manifestations of CMEs, such as loop-like ones, bubble-like ones, conic shell types, arcades of loops, or the "three-part structure", led to considerable speculation about the nature of the three-dimensional (3D) geometry (see, *e.g.*, Howard *et al.*, 1982; Fisher and Munro, 1984; Webb, 1988; Hundhausen, 1999). In recent years, a great deal of research in both modeling and observations (see, *e.g.*, Chen *et al.*, 1997, 2000; Dere *et al.*, 1999; Gibson and Low, 1998, 2000; Krall *et al.*, 2001; Cremades and Bothmer, 2004) has been focused on events having the "three-part" morphol-ogy, namely, a bright front, a dark void and a bright core of prominence material (Illing and Hundhausen, 1985). Concave-outward trailing features were noted in the SMM corona-graph images (Illing and Hundhausen, 1985); but the high-resolution LASCO observations revealed that these three-part CMEs often create the appearance of a helical or flux-rope structure.

There are two classes of flux-rope models for the origin of CMEs: one class as-sumes a preexisting flux rope (see, *e.g.*, Forbes and Isenberg, 1991; Linker *et al.*, 2003; Gibson *et al.*, 2006) and the other assumes that a flux rope is formed during the erup-tion by magnetic reconnection (Antiochos, DeVore, and Klimchuk, 1999; Amari *et al.*, 2003). In the preexisting flux-rope models, the catastrophic loss of equilibrium or ideal MHD instabilities are generally believed to be the mechanisms for triggering eruptions, and reconnection is not necessary to initiate CMEs (see, *e.g.*, Lin *et al.*, 1998; Forbes, 2000; Fan and Gibson, 2004; Török, Kliem, and Titov, 2004; Kliem and Török, 2006; Rachmeler, DeForest, and Kankelborg, 2009). In other models, such as the tether cutting (Moore and Roumeliotis, 1980) and "breakout" (Antiochos, DeVore, and Klimchuk, 1999), magnetic reconnection plays an essential role in initiating eruption. Despite the different trigger mechanisms, both models produce a flux rope after the eruption. The rapid up-ward expansion causes a vertical current sheet to form in the vicinity of the X-line be-low the eruptive field, where oppositely directed field lines reconnect yielding a highly twisted rope that escapes from the corona and soft X-ray loops or bright Hα two-ribbon flares form below, as in the standard flare model (see, *e.g.*, Kopp and Pneuman, 1976; Yokoyama and Shibata, 1998).

Based on the CME observations, basic geometric models of flux ropes using a torus geometry with its foot points remaining connected to the Sun have been developed by var-ious authors. Krall and St. Cyr (2006) (hereafter KS06) described a flux rope as having an elliptical curved axis with a circular cross section of varying radius along the axis, and the width (minor diameter) being narrowest at the foot points on the solar surface. By compar-ing an ensemble of synthetic images of flux ropes to CME observations, they found that the flux-rope model reproduced the statistical measures of a subset of flux-rope-like CMEs observed by LASCO (St. Cyr *et al.*, 2004). By assuming an electron distribution through a graduated cylindrical shell with a conical curved axis, Thernisien, Howard, and Vourlidas

(2006) created a set of synthetic images, which well reproduced the CME morphologies for 34 flux-rope-like CMEs selected from Cremades and Bothmer (2004). A more recent study (Krall, 2007) extended the work of KS06 by comparing an ensemble of synthetic images to 111 limb CMEs observed by the *Solar Maximum Mission* (SMM) (Burkepile *et al.*, 2004). Their results suggested that the flux-rope morphology can be applied not only to flux-rope-like CMEs but also to the general population of CMEs.

In this work, we apply the KS06 flux-rope model to a subset of well-observed CMEs, including flux-rope-like prominence CMEs and flare related CMEs, which are selected from the STEREO SECCHI COR1 (Howard *et al.*, 2008) preliminary event list (http://cor1.gsfc.nasa.gov/catalog). In particular, we combine 3D triangulations and the flux-rope model fit to study systematically the origin, 3D structure, and the dynamic evolution of the CMEs from COR1 and COR2 coronagraphs and EUVI images. These observations, in conjunction with SOHO LASCO observations (http://cdaw.gsfc.nasa.gov/CME_list), have been found to be extremely useful in reconstructing the 3D structures and determining the actual speeds of CMEs. This paper reports on a statistical analysis of CMEs near the solar activity minimum using the stereoscopic view of STEREO A and B. By performing a detailed investigation of CME origins, the implications on CME initiations and eruption mechanisms are discussed. The rest of the paper is organized as follows. Sections 2 and 3 describe data selection and detailed flux-rope model fitting procedures. Results of the analysis are presented in Section 4, followed by brief discussion and the scientific implications of the results in Section 5. Finally, the summary and conclusions are presented in Section 6.

2. Data Selection

COR1 and COR 2 are the Sun Earth Connection Coronal and Heliospheric Investigation (SECCHI)'s inner and outer coronagraphs onboard STEREO, whose two identical spacecraft orbit the Sun ahead (STEREO A) and behind (STEREO B) Earth near the ecliptic plane (Kaiser *et al.*, 2008). The two spacecraft separate away from Earth at a rate of about 22 degree per year. COR1 has a field of view (FOV) from 1.4 to 4 R_s (R_s is the solar radius) and the outer coronagraph COR2 FOV is from 2.5 to 15 R_s (Howard *et al.*, 2008).

We selected 27 well-observed CMEs from the COR1 preliminary event list (http://cor1.gsfc.nasa.gov/catalog) occurring from July 2007 to June 2008. We used three criteria to select the data set. These are: *i*) STEREO A and B were separated from each other by >15 degrees; *ii*) the CMEs were well observed in at least two of the three coronagraphs (STEREO A and B and/or LASCO); *iii*) the CMEs were bright enough to be observed in both COR1 and COR2 FOV. To identify the CME solar source locations and associated solar activities, we primarily identified signatures from the Extreme Ultraviolet Imager (EUVI) images. EUVI is part of the SECCHI instrument suite and observes the chromosphere and low corona in four EUV bandpasses (He II 304 Å, Fe IX 171 Å, Fe XII 195 Å, Fe XV 284 Å) out to 1.7 R_s. The EUVI images have a temporal cadence of 2.5 min in the 171 Å and 10 min in other three filters. The peak temperature response for the four bandpasses are 0.08, 1.3, 1.6 and 2.0 MK, respectively, which are capable of imaging solar structures such as filaments and prominences, coronal holes, active regions, coronal loops, coronal "bright points," *etc*. In addition, we examined the Hα and He I data from the Mauna Loa Solar Observatory (http://mlso.hao.ucar.edu), the Big Bear global Hα network (ftp://ftp.bbso.njit.edu/pub/archive), and microwave images from the Nobeyama Radio Observatory (http://solar.nro.nao.ac.jp/norh) when available. For flare identification, we use the latest event list based on recent EUV and soft X-ray imaging from LMSAL (http://www.lmsal.com/solarsoft/latest_events_archive.html).
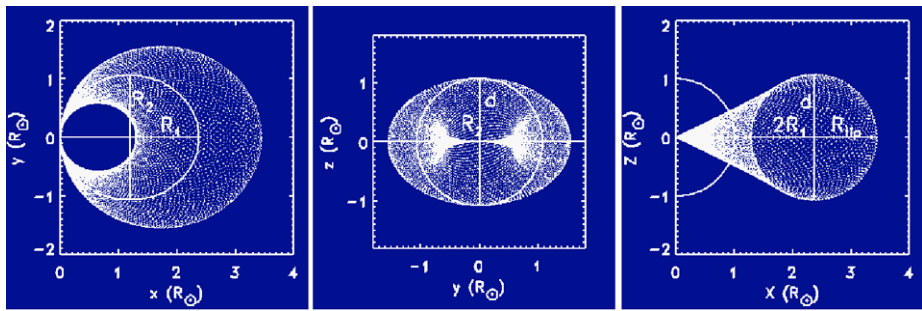
Figure 1 Illustrative plot of the flux-rope model morphology. From left to right: broadside, front (face-on), and edge-on views of a flux-rope.

3. Flux-Rope Model Fitting

The KS06 model assumes that the curved axis of the flux rope traces out an ellipse, as shown in Figure 1, with a semi-major axis of R_1 and semi-minor axis of R_2. The width of the flux rope at its apex is d. From left to right, Figure 1 gives the broadside, front (face-on), and edge-on views of the flux-rope CME, whose apex points to the west limb. The coordinate system has its origin at the solar surface, the z-axis upward, the x-axis directed toward the west limb, and the y-axis directed along the Earth–Sun line, away from Earth.

The geometry of the flux rope can be determined by two parameters: the ratio of semi-minor to semi-major axes $\lambda_\varepsilon = R_2/R_1$ and the axial aspect ratio $\Lambda_\alpha = 2R_1/d$. Note that we did not use the ellipse eccentricity here in order to fit events with $\lambda_\varepsilon > 1$. For a given pair of model parameters, the orientation angles to be varied are the source latitude and longitude (λ_0, ϕ_0) and the three tilt angles: rotation about the central axis defined by the direction of propagation (α_y), rotation of the latitude (α_x), and rotation of the longitude (α_z).

We used an iterative technique to determine the flux-rope free parameters with the procedures listed below.

i) We first performed 3D triangulation and determined the solar source location (λ_0, ϕ_0) of a CME from simultaneous STEREO A and B images from SECCHI/EUVI using the IDL SolarSoft (Bentley and Freeland, 1998) routine "scc-measure".

ii) We then determined the orientation (λ_1, ϕ_1) of a CME from simultaneous STEREO A and B images from SECCHI/COR1 or COR2. When a CME was not detectable in either STEREO A or B due to the unfavorable location of a CME (*e.g.*, near disk center or backside event), we use LASCO C2 or C3 data instead.

iii) We computed (α_x, α_z) by: $\alpha_x = \lambda_1 - \lambda_0$ and $\alpha_z = \phi_1 - \phi_0$.

iv) We determined α_y based on the neutral line orientation from the Michelson Doppler Imager (MDI), Hα filament, and/or post-flare loop observations.

v) We selected initial test values for λ_ε and Λ_α, based on measurements of (R_1, d), (R_2, R_1) or (R_2, d), depending on particular views of a CME: edge-on, broadside, or front were available. If any of these measurements was not available (*e.g.*, due to a small separation angle of A and B), we used its empirical mean value based on a previous observational flux-rope CME study.

vi) We then iteratively adjusted the initial flux-rope test parameters until a best fit to the coronagraph observations was obtained by visual examination.

Figure 2 shows an example of the flux-rope model fit for the 26 April 2008 CME. From top left to bottom right, the eight panels of Figure 2 are STEREO A and B COR1 images

Figure 2 An example of the flux-rope model fit for the 26 April 2008 CME. From top left to bottom right, the eight panels are: (a), (b), (c), and (d) STEREO A and B COR1 and EUVI 304 Å composition images at $t_1 =$ 14:45 UT, and COR2 images at $t_2 = 17:52$ UT; (e), (f), (g) and (h) STEREO A and B COR1 and COR2 images superposed with flux-rope model outline curves (yellow curves). Over-plotted yellow circles in COR1 and COR2 images indicate the Sun surface and occulting disk of COR1 and COR2, respectively.
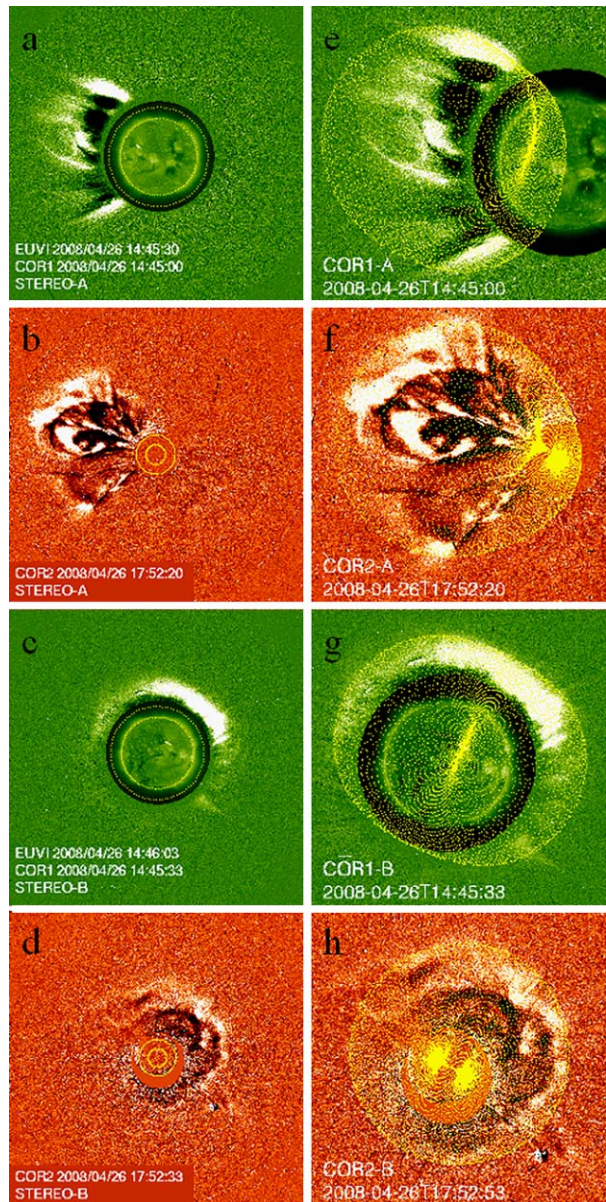
at $t_1 =$ 14:45 UT and COR2 images at $t_2 = 17:52$ UT, and superposed plots of COR1 and COR2 images with flux-rope model outline curves (yellow curves), respectively. The 26 April 2008 CME was an Earthward-directed CME, which was associated with a X-ray flare of B3.8 at N08E08. The evolution of the flare showed a clear sigmoid to arcade structure in EUVI 171 Å images, and the neutral line of the post-eruption arcade tilted $\sim 30°$ relative to the horizontal (west – east) direction. The separation angles of STEREO A and B from Earth were 25.5° and $-23.9°$, respectively, and the CME longitudes appeared in COR1 A

Table 1 Initial test parameters of the flux-rope model for the 26 April 2008 CME.

	Λ_α	λ_ε	α_y (°)	α_x (°)	α_z (°)	λ_0 (°)	ϕ_0 (°)	R_0[a] (R_s)
STEREO A	0.8	0.9	30	0	0	14	−33	1.0
STEREO B	0.8	0.9	30	0	0	14	16	1.0

[a] R_0: radius of the flux-rope origin.

Table 2 Best-fit parameters for the 26 April 2008 CME.

	Time (UT)	Λ_α	λ_ε	R_{tip}[a] (R_s)	α_y (°)	α_x (°)	α_z (°)	V_{cme}[b] (km s⁻¹)	ω_{edge}[c] (°)	ω_{broad}[d] (°)
COR1	14:45	0.5	1.2	3.5	30	−15.0	−18.0	770	62	90
COR2	17:52	0.6	0.9	15.8	30	−8.0	−12.0	770	55	71

[a] R_{tip}: radial distance from the origin to the apex of the flux rope.

[b] V_{cme}: actual speed of the CME.

[c] ω_{edge}: edge-on view CME width.

[d] ω_{broad}: broadside view CME width.

and B as E33 and W16 respectively, seen as a halo (front view) in COR1 B and a conical shape (edge-on) in COR1 A.

Based on the above observations, we set the initial test parameters of the flux-rope model for STEREO A and B as in Table 1, where R_0 is the radius of the CME origin, λ_0 and ϕ_0 are source latitude and longitude in heliocentric coordinates. By iteratively adjusting the test parameters and comparing the flux-rope models to the observed COR1 A, COR1 B, COR2 A and COR2 B images, respectively, we obtained the best-fit parameters of the flux rope as shown in Table 2, where R_{tip} is the radial distance from the origin to the apex of the flux rope. V_{cme} is the actual speed of the CME, which is given by

$$V_{cme} = \Delta(R_{tip})/dt. \tag{1}$$

ω_{edge} and ω_{broad} are the widths of the CME in edge-on view and broadside view, respectively, which are computed to be

$$\omega_{edge} = 2 \times tg^{-1}(0.5/A_\alpha),$$
$$\omega_{broad} = 2 \times tg^{-1}(\lambda_\varepsilon). \tag{2}$$

The derived actual speed of the CME is 770 km s⁻¹ and ∼1.5 times faster than the sky-plane speed of 515 km s⁻¹. The fitting results show that the CME experienced a certain amount of deflection in both latitudinal and longitudinal directions. However, it did not show rotation about its central axis, *i.e.*, α_y kept to the same value as that of the post-flare loops in this event. The CME had different widths from different perspectives. The fitted widths using COR2 images at the apex height of 15.8 R_s are slightly smaller than those using COR1 data at 3.5 R_s. This is likely because the CME has faded in intensity by the time it reached the COR2 FOV, so it was difficult to see all of the mass.

4. Statistical Analysis and Results

Table 3 summarizes the 3D properties for the 27 CMEs. Columns 1 – 6 are the number of events, CME date, and first appearance times in COR1 A and B, and longitudes of CMEs that appeared in STEREO A and B, respectively, where 'NA' indicates when a CME was too faint to give the first appearance time or not seen in either STEREO A or B, and 'DG' indicates data gap at the time of the event. Columns 7 – 11 are CME actual speeds, edge-on widths and broadside widths in COR1 FOV and COR2 FOV. Columns 12 – 13 give CME source region locations and CME orientations. Column 14 describes the types of CME solar sources and associated solar activities. Table 4 lists the best-fit parameters of the flux-rope model for COR1 and COR2 images.

4.1. Four Identified Types of CME-Related Solar Surface Activities

Using high cadence EUVI images, four types of solar surface activities are found to be associated with the CME origins: *i*) total eruptive prominence (totEP), *ii*) partially eruptive prominence (PEP), *iii*) X-ray flare (flr), and *iv*) X-type magnetic structure (X-line). Note that the above four types of solar activities are not mutually exclusive. Here the total EP refers to the case when a EP appears to escape entirely from the Sun and PEP refers to the case in which one part of the EP escapes while another remains or falls back sunward (Gilbert *et al.*, 2000). We classify a CME as a flare CME only when an A-class (or greater) X-ray flare is detected by GOES. The X-type magnetic structure indicates a magnetic X-line along which the poloidal field comes to an X-point (the axial component of the field is not necessarily zero) (see, *e.g.*, Gorbachev and Somov, 1988). It is a well-known location for current sheets and reconnections to occur and normally forms below a flux rope (*cf.* Lin *et al.*, 1998).

Figure 3 shows one example of the X-line structures associated with the 16 November 2007 CME. The CME first appeared in COR1 A FOV at ∼ 04:45 UT. A magnetic X-line (indicated by the yellow arrow in Figure 3a and 3c) started to appear as early as ∼ 23:18 UT in 15 November 2007 in EUVI A 171 Å. A prominence was observed by EUVI A 304 Å becoming active at ∼ 16:00 UT one day earlier. The X-line magnetic structure was observed to rise slowly before the CME eruption, and was well correlated with the flux-rope CME eruption observed in COR1 A in both temporal and spatial relation (Figure 3c). The associated prominence (Figure 3b) was faint and part of it was seen falling back to the solar surface during the eruption. The partial eruptive prominence, the rising of the X-line magnetic structure, and the flux-rope CME eruption can be seen more clearly in the STEREO movies (http://stereo-ssc.nascom.nasa.gov/cgi-bin/images).

Among the 27 CME events we study, 18.5% (5 of 27) are associated with total prominence eruptions, and 29.6% (8 of 27) are associated with partially erupting prominences, 26% (7 of 27) are flare related, and 26% (7 of 27) are associated with the X-type magnetic structures, and 43% (3 of 7) are associated with both X-line structures and PEP's before. Finally, there are 3 (11%) events without any detectable solar source.

4.2. Spatial Relationship Between CME Orientations and Solar Sources

It is well known that during a solar minimum, CMEs tend to be confined at low latitude (see, *e.g.*, St. Cyr *et al.*, 2000). The CMEs originating from high latitudes tend to be deflected by a strong magnetic field from polar coronal holes to lower latitudes in the inner corona (see, *e.g.*, Gopalswamy, Hanaoka, and Hudson, 2000; Gopalswamy *et al.*, 2003, 2009; Gopalswamy and Thompson, 2000; Filippov, Gopalswamy, and Lozhechkin, 2001;

Table 3 3D properties of the 27 CMEs.

No.	Date[a]	Time[b] (UT)		Long[c]		V_{cme}[d] (km s^{-1})	ω_{edge}[e] (deg)		ω_{broad}[f] (deg)		Loc$_{sr}$[g]	Loc$_{cme}$[h]	Comments[i]
		COR1 A	COR1 B	A	B		COR1	COR2	COR1	COR2			
1	08-Jul-07	16:05	16:26	E82	E64	386	42	45	84	84	S41E71	N05E71	X-line,171a[j]
2	29-Jul-07	1:15	1:26	W92	W114	752	49	49	113	100	S14W104	N02W104	Backside_flr
3	02-Aug-07	1:45	DG	E93	E70	159	35	35	84	84	N42E79	N10E79	PEP;304a
4	31-Aug-07	20:25	20:26	W61	W89	374	49	49	84	70	S25W76	S20W77	totEP, 304a&b,fw
5	08-Oct-07	11:25	9:06	W40	W75	209	64	39	84	84	N46W58	N09W63	PEP;304b
6	16-Oct-07	NA	5:26	E122	E85	147	53	49	84	84	N31E102	N19E102	PEP;195b
7	04-Nov-07	3:25	6:25	E100	E61	199	64	58	84	84	N44E80	S00E80	totEP, NoRH[k]
8	14-Nov-07	Early	Early	W38	W78	187	49	39	84	84	S29W58	S13W58	Not-detectable
9	16-Nov-07	4:45	8:26	W88	W128	352	58	53	84	84	S43W108	S04W110	X-line, 171a, w/PEP
10	25-Nov-07	18:05	17:26	E114	E73	292	49	42	84	84	N15E93	S10E93	X-line, 171b, w/PEP[l]
11	30-Nov-07	6:45	5:46	W62	W104	104	42	37	84	84	N45W83	N08W83	X-line,171&195b
12	03-Dec-07	23:45	21:26	W53	W95	217	45	42	84	84	N55W73	N08W73	X-line,171b, w/PEP
13	08-Dec-07	NA	18:45	W5	W47	529	45	37	84	84	S06W25	N08W25	Minor_flr,195b
14	16-Dec-07	NA	1:26	E132	E89	256	49	49	84	84	S31E110	S12E110	PEP;304b
15	24-Dec-07	11:25	NA	E71	E27	173	35	42	84	84	N08E49	S02E49	Not-detectable
16	31-Dec-07	1:05	1:06	E133	E89	1035	49	49	113	100	S08E97	S18E97	Flr_C8.3
17	02-Jan-08	8:45	9:06	E97	E53	850	49	49	100	96	S07E75	S08E75	Flr_C1.3
18	30-Jan-08	9:05	4:06	W33	W79	350	45	37	84	84	N50W55	N00W55	PEP, 304a&b
19	22-Mar-08	12:05	11:46	E140.5	E94	461	49	49	84	70	S14E117	S07E117	totEP, 304b
20	24-Mar-08	20:25	12:46	W20	W67	170	45	33	84	84	N40W43	N06W43	Not_detectable
21	25-Mar-08	18:55	18:55	E106	E58	1323	90	71	84	84	S10E82	S10E82	Flr_M1.7
22	05-Apr-08	15:55	16:06	W87	W135	1110	71	71	84	90	S08W111	S04W111	Flr_A3.2
23	09-Apr-08	10:05	10:16	W91	W139	691	49	49	62	53	S19W114	S32W114	totEP,304a&b[m]
24	26-Apr-08	14:15	14:26	E34	W16	770	90	71	100	84	N08E07	N00E19	Flr_B3.8

Table 3 (*Continued*)

No.	Date[a]	Time[b] (UT)		Long[c]		V_{cme}[d] (km s^{-1})	ω_{edge}[e] (deg)		ω_{broad}[f] (deg)		Loc$_{sr}$[g]	Loc$_{cme}$[h]	Comments[i]
		COR1 A	COR1 B	A	B		COR1	COR2	COR1	COR2			
25	01-Jun-08	9:05	NA	E67	E13	222	49	49	84	84	N03E38	N03E38	X-line,171a[n]
26	12-Jun-08	3:25	2:26	E115	E60	366	58	58	84	84	N50E85	N07E85	X-line,195b
27	26-Jun-08	NA	0:06	E178	E120	297	49	49	84	84	N30E146	N10E146	totEP, 304b

[a]CME date.

[b]First appearance time of CME.

[c]CME longitude as seen in STEREO A and B.

[d]CME actual speed.

[e]CME width as seen edge-on.

[f]CME width as seen in broadside view.

[g]CME source location from Earth view.

[h]CME orientation as measured in COR2 FOV.

[i]Comments on CME types, imager sources, and solar activities. EP = erupting prominence; totEP = total EP; PEP = partially EP; flr = flare; w/ = with; fw = fast and wide.

[j]Accompanied with brightening and sunward EP in the vicinity of the X-line.

[k]EP was detected by Nobeyama radioheliograph.

[l]Accompanied with PEP, which erupted one day earlier.

[m]The observed EP was bright and twisted with possible kink instability involved.

[n]The X-line type structure started rising ∼24 hours ago.

Table 4 Flux-rope model best-fit parameters for COR1 and COR2 data.

No.[a]	Date	t_1 (UT)	R_{tip1} (R_s)	$\Lambda_{\alpha 1}$	$r_{\varepsilon 1}$	α_{y1} (°)	t_2[b] (UT)	R_{tip2} (R_s)	$\Lambda_{\alpha 2}$	$r_{\varepsilon 2}$	α_{y2} (°)	R_0 (R_s)
1	08-Jul-2007	18:25	2.5	1.3	0.9	−15.9	23:52	13.4	1.2	0.9	−15.9	1.13
2	29-Jul-2007	01:46	2	1.1	1.5	89.4	04:23	12.2	1.1	1.2	89.4	0.5
3	02-Aug-2007	04:45	1.5	1.6	0.9	8.9	10:52	6.5	1.6	0.9	8.9	1.1
4	31-Aug-2007	21:40	2.2	1.1	0.9	64.9	23:52	6.5	1.1	0.7	64.9	1
5	08-Oct-2007	13:00	1.6	0.8	0.9	−13.3	21:52	11.2	1.4	0.9	−13.3	1
6	16-Oct-2007	16:25	1.4	1	0.9	13.2	06:52[b]	12.3	1.1	0.9	21.8	1
7	04-Nov-2007	12:05	2.6	0.8	0.9	0	23:22	14.2	0.9	0.9	0.2	1
8	14-Nov-2007	14:05	1.6	1.1	0.9	25.4	02:22[b]	13.4	1.4	0.9	25.4	1
9	16-Nov-2007	10:45	2.9	0.9	0.9	−13.5	15:52	12.1	1	0.9	−13.5	1.15
10	26-Nov-2007	04:45	2.7	1.1	0.9	7.4	08:52	8.9	1.3	0.9	7.4	1.19
11	30-Nov-2007	14:05	1.7	1.3	0.9	10.3	12:22[b]	13.6	1.5	0.9	10.3	1.2
12	04-Dec-2007	05:20	1.9	1.2	0.9	−10.9	16:52	14.8	1.3	0.9	−10.9	1.15
13	08-Dec-2007	21:25	3.5	1.2	0.9	−6.2	22:22	6.1	1.5	0.9	−6.2	1
14	16-Dec-2007	09:25	3.1	1.1	0.9	−9.9	17:22	13.6	1.1	0.9	−15.9	1
15	24-Dec-2007	20:55	2.8	1.6	0.9	−3.5	09:52[b]	14.3	1.3	0.9	−3.5	1
16	31-Dec-2007	01:20	2.2	1.1	1.5	75.6	02:52	10.4	1.1	1.2	75.6	1
17	02-Jan-2008	11:05	3.5	1.1	1.2	40.9	13:22	13.5	1.1	1.1	40.6	1
18	30-Jan-2008	09:15	3	1.2	0.9	6.3	14:22	12.2	1.5	0.9	6.3	1
19	22-Mar-2008	16:00	1.9	1.1	0.9	84.8	19:22	9.9	1.1	0.7	84.8	1
20	24-Mar-2008	19:50	1.9	1.2	0.9	1.6	08:52[b]	13.4	1.7	0.9	1.9	1
21	25-Mar-2008	19:25	2.6	0.5	0.9	0	20:22	9.1	0.7	0.9	0	1
22	05-Apr-2008	16:05	1.6	0.7	0.9	0.1	17:52	11.8	0.7	1	0	1
23	09-Apr-2008	10:45	1.8	1.1	0.6	76.7	13:52	12.9	1.1	0.5	82.1	1
24	26-Apr-2008	14:45	3.5	0.5	1.2	30	17:52	15.8	0.7	0.9	30	1
25	02-Jun-2008	03:22	6.1	1.1	0.9	20.4	08:22	11.8	1.1	0.9	20.4	1
26	12-Jun-2008	06:05	3.1	0.9	0.9	−20	11:23	13.1	0.9	0.9	−20	1.1
27	26-Jun-2008	01:45	1.5	1.1	0.9	−6.4	09:23	13.2	1.1	0.9	−2.4	1

[a]Column 1: Number of events. Column 2: CME date. Columns 3 – 7: time, R_{tip}, Λ_α, r_ε, α_y for COR1 images. Columns 8 – 12: time, label b indicates time on the following day than shown in column 2; R_{tip}, Λ_α, r_ε, α_y for COR2 images. Column 13: the radius of the flux-rope origin.

Plunkett *et al.*, 2001; Cremades, Bothmer, and Tripathi, 2006). Figure 4 shows an illustrative example of the deflection of the 30 January 2008 CME. The CME was associated with an EP at N50W55, which became active as early as 01:00 UT in STEREO B EUVI 304 Å, and started erupting non-radially at ∼ 02:00 UT. The flux-rope CME appeared above the northwest limb at ∼ 04:00 UT in COR1 B, deflecting towards the low-latitudes streamer belt in the first few solar radii, and then continued to propagate in a radial direction throughout COR1 FOV, as shown in Figure 4a – d. In Figure 4e – h we present COR1 (running difference images (e, f) and origin images (g, h)) and EUVI 304 Å composition images together with extrapolated magnetic field lines from the global PFSS model based on Wilcox Solar Observatory (WSO) data (http://wso.stanford.edu/Harmonic.los/ghlist.html). Figure 4e – f show COR1 running difference images at 05:40 UT and 09:25 UT, respectively, which allow us to see more clearly how the CME fronts (labeled by orange arrows) deflect towards

Figure 3 (a) An X-type magnetic structure (yellow arrow) which is associated with the 16 November 2007 CME appeared in STEREO A EUVI 171 Å at 03:53:30 UT, (b) observed prominence in STEREO A EUVI 304 Å at 03:56:15 UT, (c) Superposition images of STEREO A COR1 and EUVI 171 Å and (d) STEREO A EUVI 304 Å, which show good correlations between the associated solar activity features and the CME eruption.
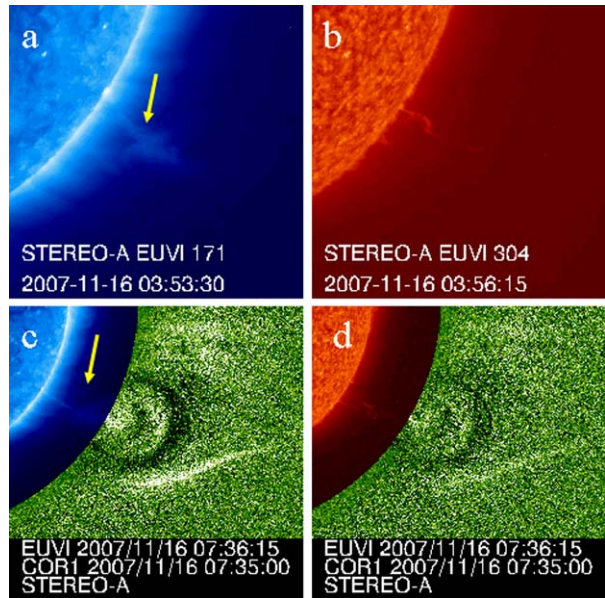
lower latitudes along the outskirt field line of the helmet steamer belt. Figure 4g–h show the locations of the streamer belts above limb (indicated by yellow arrows) in the COR1 origin images.

To study the relationship between the deflection of a CME and the latitudinal distance of its source away from the corresponding steamer belt, we use the WSO source surface synoptic charts ($R = 2.5$ radial model) (http://wso.stanford.edu/synsourcel.html) to obtain the streamer belt neutral line location, as shown in Figure 5, where we over-plotted the CME source region (black circle in upper right corner) in the corresponding synoptic chart. The latitudinal distance between the CME source and the streamer belt neutral line is computed as $|\text{Lat}_{sr} - \text{Lat}_{nl}|$, where Lat_{sr} and Lat_{nl} denote the latitudes of the CME source and the streamer belt neutral line.

Figure 6 shows (a) the distribution of the CME source regions, and (b) the distribution of the CME orientations, superposed with the locations of streamer belts. The CME source regions and orientations are obtained from Table 3 columns 12 and 13, respectively. From Figure 6a, we can see that the CME source regions (circles) are widely scattered over the whole solar surface whereas the CME orientations (triangles) and streamer belt locations (cross signs) tend to group together (Figure 6b).

Further examinations indicate that the deflections of slow CMEs with $V \leq 400$ km s^{-1} appear to be well correlated to the latitudinal distances between their source regions and streamer belts with a correlation coefficient of $r = 0.92$ (Figure 7a), while there is no such correlation for faster CMEs with $V > 400$ km s^{-1} (Figure 7b). Furthermore, the deflections of slow CMEs are generally larger than those of fast CMEs, as shown in Figure 8. The mean deflections for slow and fast CMEs are 28° and 8°, and the mean latitudinal deviations between the CME orientations and streamer belts are 6° and 17°, respectively.

The above result is consistent with Yashiro *et al.* (2008) report of a statistical study on the spatial relationship between solar flares and CMEs that found the flare–CME geometric relation to be different between weak (C-class) and strong (X-class) events. For C-class events, the flare source positions were widely scattered with respect to the CME central lo-
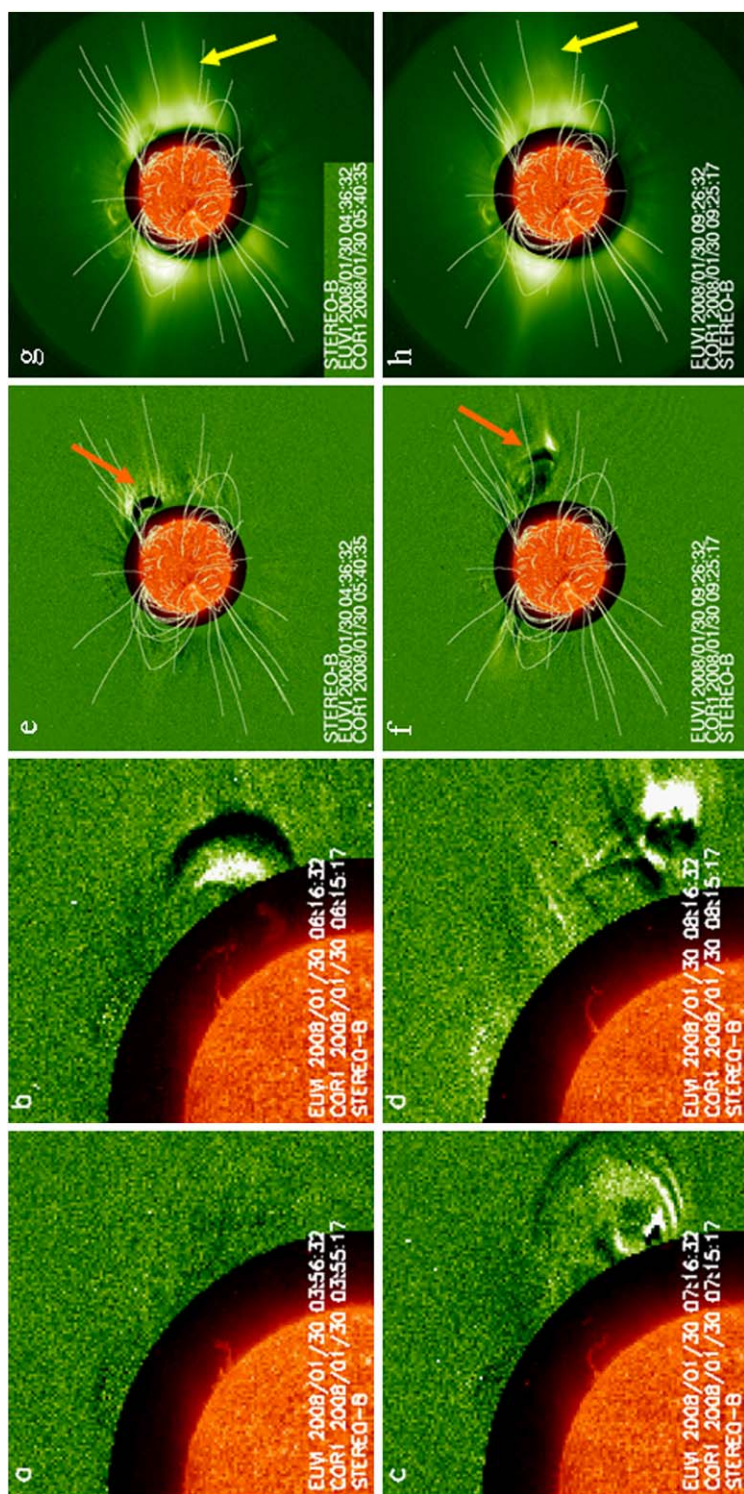
Figure 4 COR1 and EUVI 304 Å composition images of the 30 January 2008 CME together with magnetic field lines from the global PFSS model, showing the evolution of the deflecting flux-rope CME and its associated erupting prominence.
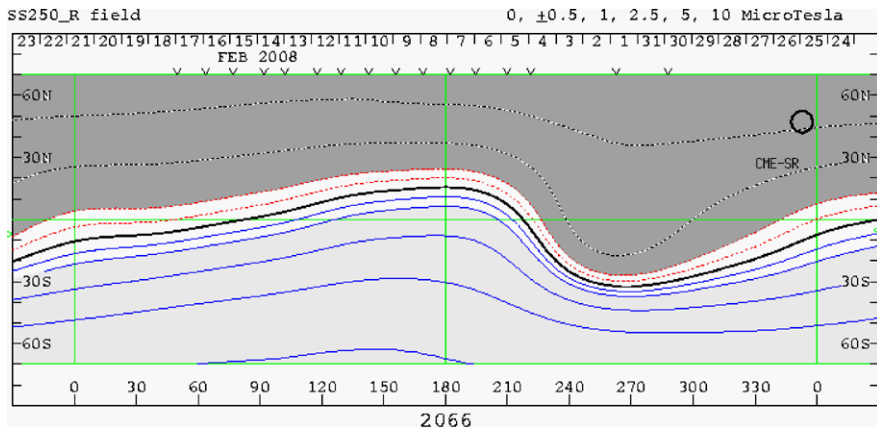
Figure 5 WSO source surface synoptic chart over-plotted with the 30 January 2008 CME source region (black circle in upper right corner) to study the latitudinal distance between the CME source and the streamer belt.

Figure 6 (a) Distribution of the CME source regions, and (b) distribution of the CME orientations, superposed with the locations of streamer belts for the 27 CMEs.
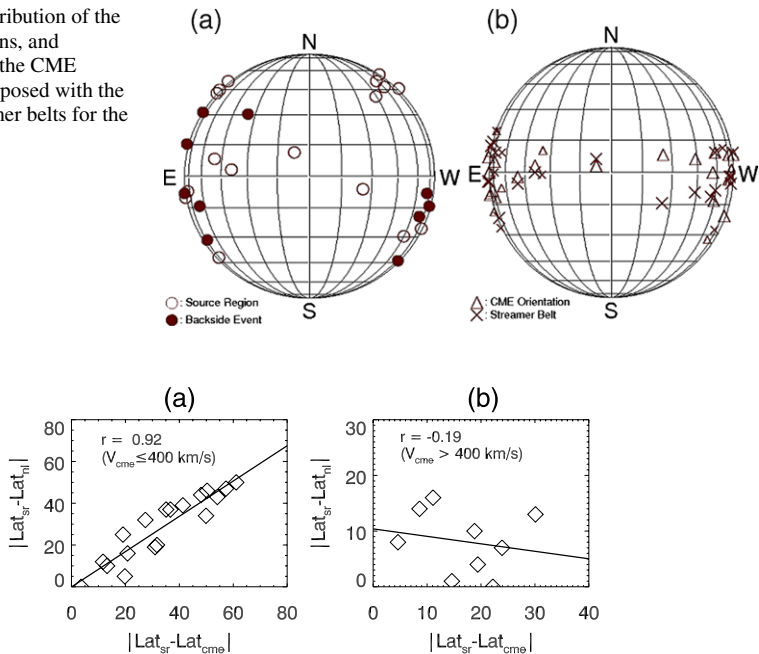
Figure 7 Correlation between the deflections of CMEs and the latitudinal distances of their source regions away from streamer belts for (a) 18 weak CMEs with $V \leq 400 \ \mathrm{km \, s^{-1}}$, and (b) 9 strong CMEs with $V > 400 \ \mathrm{km \, s^{-1}}$. $\mathrm{Lat_{sr}}$, $\mathrm{Lat_{cme}}$, and $\mathrm{Lat_{nl}}$ denote the latitudes of solar source, CME orientation, and streamer belt neutral line, respectively.

cations, while for X-class events, most of the flares lie under the CME span center. This may indicate that weak CMEs are more easily deflected by the ambient magnetic field structures (see, *e.g.*, Moore and Sterling, 2007).

Figure 8 Histograms of the deviations between CME sources and CME orientations for (a) 18 weak CMEs ($V \leq 400$ km s^{-1}), and (c) 9 strong CMEs with $V > 400$ km s^{-1}; and histograms of the deviations between CME orientations and streamer belts for (b) 18 weak CMEs, and (d) 9 strong CMEs. Lat$_{sr}$, Lat$_{cme}$, and Lat$_{nl}$ denote the latitudes of solar source, CME orientation, and streamer belt neutral line, respectively.
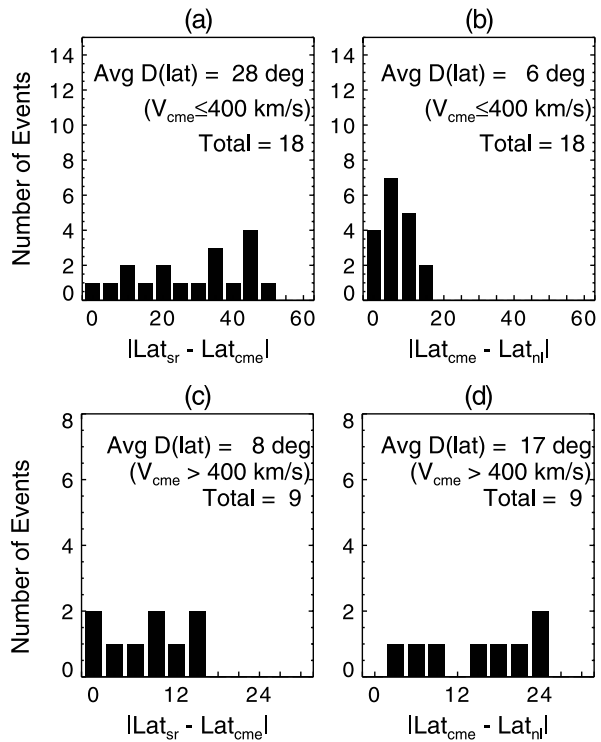
4.3. Actual Speed and Width Distributions of the CMEs

Using the flux-rope model fitting procedures described in Section 3, we obtained the actual speeds, edge-on widths, and broadside widths of the 27 CMEs, as listed in Table 3. Figures 9 and 10 show the scatter plot and the histogram of the CME actual speeds, respectively. We have divided the CMEs into five groups: (a) totEP-CME, (b) PEP-CME, (c) flare CME (flr-CME), (d) X-line type CME (X-line-CME) and (e) no source CME (NA-CME). The mean values of the actual speeds for the five groups are 404 km s^{-1}, 247 km s^{-1}, 909 km s^{-1}, 276 km s^{-1}, and 176 km s^{-1}. Among the total of 27 CMEs, the 25 March 2008 CME is the fastest CME with an actual speed of 1323 km s^{-1}, which is associated with an M1.7 flare at S10E82. The slowest CME (the 30 November 2007 CME) is in the X-line type group with a speed of 104 km s^{-1}. There are 37.5% (3 of 8) PEP CMEs or 43% (3 of 7) X-line CMEs associated with both X-line structures and PEPs. The mean actual speed of the X-line type CMEs (276 km s^{-1}) is similar to that of the PEP-CMEs (247 km s^{-1}), whereas totEP-CMEs have a much higher mean value of 404 km s^{-1}. The three CMEs with no detectable sources are the weakest with a mean speed of 176 km s^{-1}.

   Figure 11 shows the histograms of broadside and edge-on width distributions of the CMEs in COR1 FOV and COR2 FOV, respectively. The broadside and edge-on widths are computed using Equation (2) in Section 3. All the 27 events were measured at leading-edge heights ranging from 2.0 to 3.5 R_s in COR1 and from 7.5 to 14.5 R_s in COR2. The mean values of the width distribution for Figure 11a (COR1 edge-on width), Figure 11b (COR1 broadside width), Figure 11c (COR2 edge-on width), and Figure 11d (COR2 broadside width) are 52, 86, 48, and 83 degrees, respectively. Both broadside widths and edge-on widths measured within COR1 and COR2 FOV are roughly self-similar. The average mean

Figure 9 Scatter plot of the actual speed distribution for the 27 CMEs. The numbers on the *X* axis are the event numbers for each one of the five sub-groups.
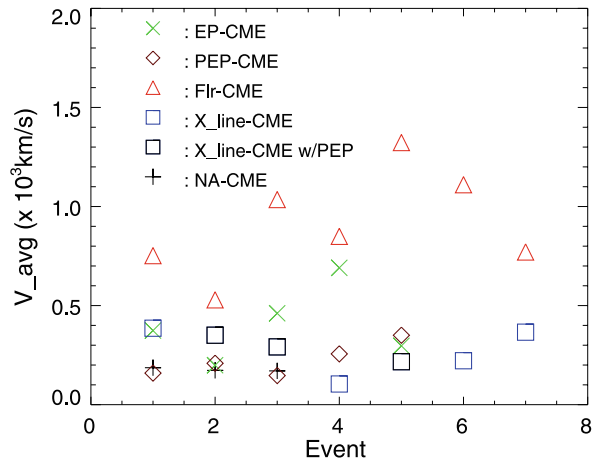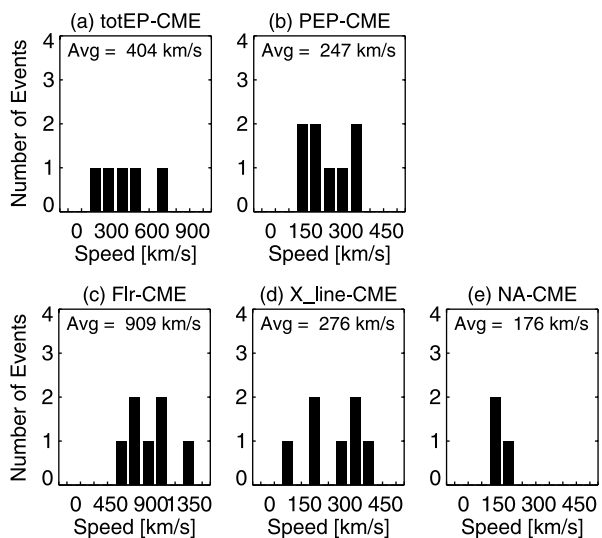

Figure 10 Histogram of the actual speed distribution for (a) total EP-CMEs, (b) partial EP-CMEs, (c) flare-CMEs, (d) X-line type CMEs, and (e) no-source CMEs.

values of edge-on and broadside widths for the 27 CMEs are 52 and 85 degrees, respectively. Note that the widths in COR2 FOV are slightly smaller than those in COR1 FOV, which is likely due to: *i*) the CMEs having faded in intensity by the time they got to COR2, so it was harder to see all of the mass, and *ii*) the ratios Λ_α and λ_ε decreasing as the flux rope rises and stretches out its lower current sheet (or becomes totally detached).

The obtained widths are in agreement with the results from St. Cyr *et al.* (2004); they identified 27 LASCO flux-rope-like CMEs within 30° from the limb and found that the average angular width was 48° ± 12° for the axis events and 78° ± 17° for the broadside events. However, St. Cyr *et al.* (1999) reported an average expansion of ∼10° as the width for CMEs observed by MLSO and SMM. This is because the widths in St. Cyr *et al.* (1999) were measured assuming that CMEs originate from the center of the Sun (instead of near the solar surface as in the flux-rope model), which causes underestimation of widths for CMEs observed in the lower corona.

Figure 11 Histograms of broadside and edge-on width distributions of the CMEs: (a) COR1 edge-on widths, (b) COR1 broadside widths, (c) COR2 edge-on widths, and (d) COR2 broadside widths.
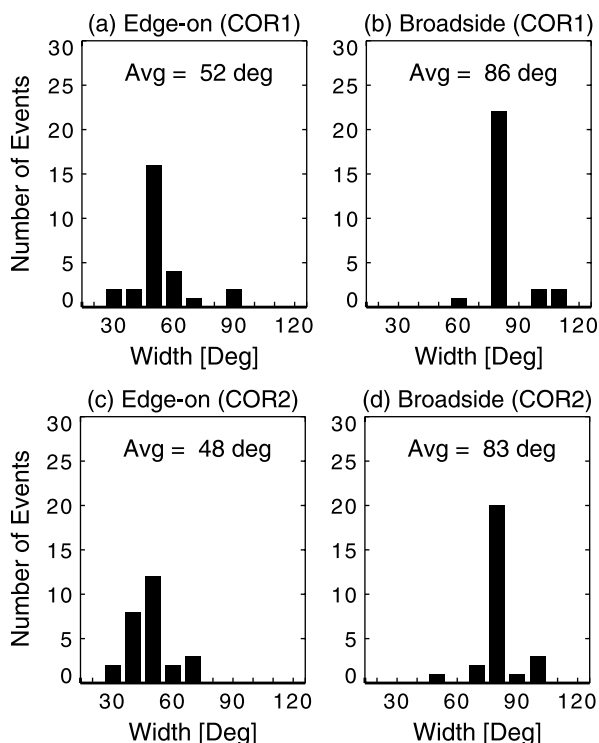
5. Discussion

5.1. Direct Observations of the X-type Magnetic Structures from EUVI

SECCHI/EUVI instruments have unprecedented capabilities to identify CME source regions, providing almost uninterrupted full-disk imaging with high cadences. A striking finding of this work is the direct detection of the X-type magnetic structures by EUVI 171 Å and/or EUVI 195 Å as a common precursor (26%: 7 of 27 events) for the CME eruptions. The X-type magnetic structures were observed either to rise slowly before and/or during the CME eruptions, or to be stationary and accompanied by minor brightening and/or downward flows. They are normally faint features and can only be detected above limb, and occasionally accompanied with PEP. The associated CME eruptions have a slow and long duration acceleration phase and its average actual speed was found to be similar to the PEP CMEs (see Figure 9). No typical evidence of reconnection, such as X-ray or Hα flares, was detected in these events, except that in the 8 July 2008 event (Figure 3) a minor brightening was observed. It is not clear whether the magnetic reconnection features are too faint to be observed in these cases or if the magnetic reconnection did not occur due to lack of favorable conditions, *e.g.*, the growth of the local current density and the development of anomalous resistivity in the vicinity of the X-line (Titov, Galsgaard, and Neukirch, 2003). Our work is the first statistical study on such X-line type CMEs in EUV near a solar minimum. Although statistical studies of observed post-CME current sheet structures have been performed using SOHO LASCO and UVCS data (see, *e.g.*, Webb *et al.*, 2003; Ciaravella and Raymond, 2008), there are no statistical studies of the pre-CME X-type magnetic structures in EUV (see, *e.g.*, Yokoyama *et al.*, 2001) prior to STEREO. One possible

reason might be due to the low cadence of the EIT instrument and the limited FOV of TRACE images.

5.2. Spatial Relationship Between CME Orientations and Their Sources

Our quantitative analysis has confirmed that slow CMEs near a solar minimum with $V \leq 400 \text{ km s}^{-1}$ tend to deflect towards and propagate along the directions of streamer belts. However, it is also found that for fast CMEs with $V > 400 \text{ km s}^{-1}$, which are related to X-ray flares or occur near active regions, the deflections are small and seem to be more likely controlled by the intrinsic magnetic structures of the ambient active regions. Using the 9 April 2008 CME as an example, a deflection toward the opposite direction of the streamer belt was detected, with the CME and the streamer belt located at S32W114 and N12W114, respectively. This CME was associated with a bright twisted EP originated from S19W114 at AR10997, with a likely kink instability involved, and it produced an actual speed of 690 km s^{-1}. We do not have an explanation of why the CME was deflected toward the opposite direction of the streamer belt, although it may be related to the complex magnetic structures inside or near the active region, including large low-latitude coronal holes (*cf.* Gopalswamy *et al.*, 2009).

5.3. Three-dimensional Reconstructions of CMEs

The 3D reconstruction of CMEs using the flux-rope geometry model achieves the best result when two orthogonal views of a CME are available, namely, seen edge-on (or broadside) in one spacecraft and face-on in another. Such cases occur when STEREO A and B are separated with 90°, as shown in Figure 1, where we can easily measure and fit the flux-rope parameters. In the 26 April 2008 CME (Figure 2), when the CME deviated from LOS in both latitude and longitude, the estimation of the initial test parameters of a flux-rope CME was improved by a two-step procedure. *i*) First, we determined test values using an elliptical cone model fit to the partial halo (Figure 2b). *ii*) We applied the iterative method to get the best fit parameters. By replacing the second and third equations in (4) of Xie, Ofman, and Lawrence (2004) with elliptical parametric equations, our cone model can be adapted to an elliptical cone model in a quite straightforward manner. Although the elliptical cone model and flux-rope model have different internal structures, they have similar profiles (projections) in both front and side views. For small separation angle cases, as in the early STEREO mission, the flux-rope model yields the best fit parameters in only one perspective view: broadside or edge-on, depending on particular images, leaving parameters in the other view unresolved. The results of this study are preliminary; we intend to extend this work to a significantly larger sample in the future.

6. Summary and Conclusions

This is the first statistical study on CMEs using the stereoscopic views of STEREO A and B. We reported on the origin, 3D structure, and the dynamic evolution of 27 CMEs using the Krall and St. Cyr (2006) flux-rope model. This work has yielded the following results.

1. Four types of solar sources have been identified to be associated with CME origins: *i*) total eruptive prominence (totEP), *ii*) partially eruptive prominence (PEP), *iii*) X-ray flare, and *iv*) X-type magnetic structure. Among the 27 CMEs, 18.5% (5 of 27) are associated with total EPs, and 29.6% (8 of 27) are associated with partial EPs. 26% (7 of 27)

are flared related, and 26% are associated with X-line type, and 43% (3 of 7) are associated with both X-line structures and PEPs. There are 3 (11%) faint and weak CMEs ($V < 200$ km s^{-1}) without any detectable solar sources.

2. Weak CMEs with $V \leq 400$ km s^{-1} tend to deflect towards and propagate along the streamer belts, apparently due to the deflection by the diverging, strong polar magnetic fields of the corona holes. There is a good correlation between the deflections of CMEs and the distances of their source from the streamer belts for the 18 weak CMEs. For strong CMEs with $V > 400$ km s^{-1} (seven flr-CMEs plus two fast totEP-CMEs) there is no such a correlation. Instead, their deflections are distributed randomly with respect to the latitudinal distances of their sources from the streamer belt locations, and some events even show opposite deflections, away from the streamer belts.

3. The actual speed distributions of the CMEs show that the mean values for four groups of CMEs: totEP-CME, PEP-CME, flr-CME, and X-line-CME are 404 km s^{-1}, 247 km s^{-1}, 909 km s^{-1}, and 276 km s^{-1}, respectively. The flr-CME group is the fastest, and the X-line-CMEs and PEP-CMEs have the similar mean values of 247 km s^{-1} and 276 km s^{-1}.

4. The CMEs have different widths from different views. The mean values of edge-on and broadside widths in COR1 and COR2 are 56, 86, 48, and 83 degrees, respectively, suggesting a roughly self-similar expansion of the CMEs.

5. The KS06 flux-rope geometry model has been shown again to possess the potential to reconstruct a more realistic CME morphology than the CME cone model for both prominence CMEs that have different edge-on and broadside widths and bubble-like flare related CMEs.

References

Amari, T., Luciani, J.F., Aly, J.J., Mikic, Z., Linker, J.: 2003, *Astrophys. J.* **585**, 1073.
Antiochos, S.K., DeVore, C.R., Klimchuk, J.A.: 1999, *Astrophys. J.* **510**, 485.
Bentley, R., Freeland, S.: 1998, In: *Crossroads for European Solar and Heliospheric Physics. Recent Achievements and Future Mission Possibilities*, Puerto de la Cruz, Tenerife, Canary Islands, Spain, March 23–27, 1998. Organised by ESA Solar Physics Planning Group (SPPG) and Instituto de Astrofisica de Canarias (IAC). European Space Agency, 225.
Brueckner, G.E., Howard, R.A., Koomen, M.J., Korendyke, C.M., Michels, D.J., Moses, J.D., Socker, D.G., Dere, K.P., Lamy, P.L., Llebaria, A., *et al.*: 1995, *Solar Phys.* **162**, 357.
Burkepile, J.T., Hundhausen, A.J., Stanger, A.L., St. Cyr, O.C., Seiden, J.A.: 2004, *J. Geophys. Res.* **109**, A03103.
Chen, J., Howard, R.A., Brueckner, G.E., Santoro, R., Krall, J., Paswaters, S.E., St. Cyr, O.C., Schwenn, R., Lamy, P., Simnett, G.M.: 1997, *Astrophys. J.* **490**, L191.
Chen, J., Santoro, R.A., Krall, J., Howard, R.A., Duffin, R., Moses, J.D., Brueckner, G.E., Darnell, J.A., Burkepile, J.T.: 2000, *Astrophys. J.* **533**, 481.
Ciaravella, A., Raymond, J.C.: 2008, *Astrophys. J.* **686**, 1372.
Cremades, H., Bothmer, V.: 2004, *Astron. Astrophys.* **422**, 307.
Cremades, H., Bothmer, V., Tripathi, D.: 2006, *Adv. Space Res.* **38**, 461.
Dere, K.P., Brueckner, G.E., Howard, R.A., Michels, D.J.: 1999, *Astrophys. J.* **516**, 465.
Fan, Y., Gibson, S.E.: 2004, *Astrophys. J.* **609**, 1123.
Filippov, B.P., Gopalswamy, N., Lozhechkin, A.V.: 2001, *Solar Phys.* **203**, 119.
Fisher, R.R., Munro, R.H.: 1984, *Astrophys. J.* **280**, 428.
Forbes, T.G.: 2000, *J. Geophys. Res.* **105**, 23153.

Forbes, T.G., Isenberg, P.A.: 1991, *Astrophys. J.* **373**, 294.

Gibson, S.E., Low, B.C.: 1998, *Astrophys. J.* **493**, 460.

Gibson, S.E., Low, B.C.: 2000, *J. Geophys. Res.* **105**, 18187.

Gibson, S.E., Foster, D., Burkepile, J., de Toma, G., Stanger, A.: 2006, *Astrophys. J.* **641**, 590.

Gilbert, H.R., Holzer, T.E., Low, B.C., Burkepile, J.T.: 2000, *Astrophys. J.* **549**, 1221.

Gopalswamy, N., Thompson, B.J.: 2000, *J. Atmos. Solar Terr. Phys.* **62**, 1457.

Gopalswamy, N., Hanaoka, Y., Hudson, H.S.: 2000, *Adv. Space Res.* **25**, 1851.

Gopalswamy, N., Shimojo, M., Lu, W., Yashiro, S., Shibasaki, K., Howard, R.A.: 2003, *Astrophys. J.* **586**, 562.

Gopalswamy, N., Mäkelä, P., Xie, H., Akiyama, S., Yashiro, S.: 2009, *J. Geophys. Res.* **114**, A00A22.

Gorbachev, V.S., Somov, B.V.: 1988, *Solar Phys.* **117**, 77.

Howard, R.A., Michels, D.J., Sheeley, N.R. Jr., Koomen, M.J.: 1982, *Astrophys. J.* **263**, L101.

Howard, R.A., Moses, J.D., Vourlidas, A., Newmark, J.S., Socker, D.G., Plunkett, S.P., Korendyke, C.M., Cook, J.W., Hurley, A., Davila, J.M., *et al.*: 2008, *Space Sci. Rev.* **136**, 67.

Hundhausen, A.J.: 1999, In: Strong, K.T., *et al.* (eds.) *Coronal Mass Ejections, in the Many Faces of the Sun*, Springer, New York, 143.

Illing, R.M.E., Hundhausen, A.J.: 1985, *J. Geophys. Res.* **90**, 275.

Kaiser, M.L., Kucera, T.A., Davila, J.M., St. Cyr, O.C., Guhathakurta, M., Christian, E.: 2008, *Space Sci. Rev.* **136**, 5.

Kliem, B., Török, T.: 2006, *Phys. Rev. Lett.* **96**, 255002.

Krall, J.: 2007, *Astrophys. J.* **657**, 559.

Krall, J., St. Cyr, O.C.: 2006, *Astrophys. J.* **652**, 1740.

Krall, J., Chen, J., Duffin, R.T., Howard, R.A., Thompson, B.J.: 2001, *Astrophys. J.* **562**, 1045.

Kopp, R.A., Pneuman, G.W.: 1976, *Solar Phys.* **50**, 85.

Lin, J., Forbes, T.G., Isenberg, P.A., Démoulin, P.: 1998, *Astrophys. J.* **504**, 1006.

Linker, J.A., Mikic, Z., Lionello, R., Riley, P., Amari, T., Odstrcil, D.: 2003, *Phys. Plasmas* **10**, 1971.

Moore, R.L., Sterling, A.C.: 2007, *Astrophys. J.* **661**, 543.

Moore, R.L., Roumeliotis, G.: 1980, In: Svestka, Z., Jackson, B.V., Machado, M.E. (eds.) *Eruptive Solar Flares, IAU Colloq.* **133**, 69.

Plunkett, S.P., Thompson, B.J., St. Cyr, O.C., Howard, R.A.: 2001, *J. Atmos. Solar Terr. Phys.* **63**, 389.

Rachmeler, L.A., DeForest, C.E., Kankelborg, C.C.: 2009, *Astrophys. J.* **693**, 1431.

St. Cyr, O.C., Burkepile, J.T., Hundhausen, A.J., Lecinski, A.R.: 1999, *J. Geophys. Res.* **104**, 12493.

St. Cyr, O.C., Plunkett, S.P., Michels, D.J., Paswaters, S.E., Koomen, M.J., Simnett, G.M., Thompson, B.J., Gurman, J.B., Schwenn, R., Webb, D.F., *et al.*: 2000, *J. Geophys. Res.* **105**, 18169.

St. Cyr, O.C., Cremades, H., Bothmer, V., Krall, J., Burkepile, J.T.: 2004, In: *AGU 2004 Fall Meeting*, abstract SH22A-04.

Thernisien, A.F.R., Howard, R.A., Vourlidas, A.: 2006, *Astrophys. J.* **652**, 763 – 773.

Titov, V.S., Galsgaard, K., Neukirch, T.: 2003, *Astrophys. J.* **582**, 1172.

Török, T., Kliem, B., Titov, V.S.: 2004, *Astron. Astrophys.* **413**, L27.

Webb, D.F.: 1988, *Astrophys. J.* **93**, 1749.

Webb, D.F., Burkepile, J., Forbes, T.G., Riley, P.: 2003, *J. Geophys. Res.* **108**, 1440.

Xie, H., Ofman, L., Lawrence, G.: 2004, *J. Geophys. Res.* **109**, A03109.

Yashiro, S., Michalek, G., Akiyama, S., Gopalswamy, N., Howard, R.A.: 2008, *Astrophys. J.* **673**, 1774.

Yokoyama, T., Shibata, K.: 1998, *Astrophys. J.* **494**, L113.

Yokoyama, T., Akita, K., Morimoto, T., Inoue, K., Newmark, J.: 2001, *Astrophys. J.* **546**, L69.